https://doi.org/10.5194/wes-2026-150
Preprint. Discussion started: 18 September 2026

eawe european academy of wind energy
Open Access WIND ENERGY SCIENCE DISCUSSIONS

Using an Airborne Wind Energy System as a turbulence sensor

Agustí Porta Ko[1,2], Mark Kelly[1], Duc H. Nguyen[3], and Espen Oland[2]

[1]Department of Wind and Energy Systems; Risø Campus, Danish Technical University; Roskilde 4000 Denmark.
[2]Kitemill AS; Voss, 5704, Norway.
[3]School of Civil, Aerospace, and Design Engineering; University of Bristol; Bristol, BS8 1TR, United Kingdom

Correspondence: Agustí Porta Ko (apoko@dtu.dk, apo@kitemill.com)

Abstract.

Atmospheric turbulence characterisation in the upper atmospheric boundary layer (ABL) remains a challenge, as conventional measurement techniques, such as masts and lidars, have fundamental limitations at those altitudes. Airborne Wind Energy Systems (AWES), which operate tethered kites at altitudes beyond the surface-layer, show great promise as turbulence sensing platforms. This paper describes a methodology to characterise atmospheric turbulence from quantities that are available from standard onboard sensors. The methodology has been developed in UniSimAWE, Kitemill's in-house simulator framework, where the Mann model has been employed to generate atmospheric turbulence. The two operational phases of ground generation AWES, production and return phase, have been exploited as complementary sampling strategies. During the return phase, the kite follows a near-streamwise trajectory, enabling measurement of the turbulence intensity and integral time and length scales for the three velocity components. Moreover, Taylor's frozen turbulence hypothesis has been shown to hold for this sampling strategy, both through the integral length-to-time scale ratio, and the wavenumber-to-frequency power spectral density ratio. In the production phase, the kite flies in crosswind manoeuvres, following a helical path; the dominant crosswind component allows measurement of the integral time and length scales in the crosswind direction which are unavailable from conventional fixed-point sensors. In addition, the helical path enables the measurement of streamwise integral time scale. A novel time scale is introduced to characterise the interaction between the atmospheric turbulent structures and the AWES trajectory, with relevance for turbulence-adaptive control. The results demonstrate the potential of AWES to measure relevant atmospheric turbulence quantities throughout its operation, with advantages over conventional measurement techniques.

1 Introduction

Measurement of turbulence in the upper atmospheric boundary layer (ABL) has essentially remained an open topic for decades, due to persistent limitations of available measurement technologies. Measurement masts rarely exceed 100–150 m height, which is basically the upper limit of the depth of the surface-layer, where the surface-dominated flow physics are well understood. Radiosondes and balloons measure too infrequently, also typically not averaging long enough at a given height to reliably capture turbulence statistics. The emergence and maturation of lidar has helped with the measurement of mean winds above the surface layer. However, turbulence measurements by lidar have remained problematic, worsening with increasing height away from the Earth's surface (Eberhard et al., 1989; Smalikho and Banakh, 2017). The latter aspect is related, but not limited, to the increasing size of averaging volume with height; compared to conventional measurements, large biases and uncertainties emerge due to multiple mechanisms (Peña et al., 2025). Airborne Wind Energy Systems (AWES) on the other hand enable repeated looping path sampling with resolutions of several meters, much finer than lidar, thus showing new promise in measuring turbulence through the ABL. Moreover, the looping path by AWES allows for turbulence characterisation in spatial directions that are not available by fixed-point measurement techniques, further illustrating AWES' potential to measuring atmospheric turbulence.

AWES have been explored as atmospheric sensing platforms; early work by Ranneberg (2013) demonstrated that wind speed can be inferred from kite dynamics and tether force measurements, validated against lidar observations. Schmidt et al. (2017, 2020) extended this idea through extended Kalman filtering approaches combining kite dynamics with reference wind measurements to estimate atmospheric wind conditions during flight. More recently, Cayon et al. (2025) presented a "kite-as-a-sensor" framework using a soft-wing AWES and standard onboard measurements to reconstruct wind speed and direction through sensor fusion, with good agreement against lidar observations. While these studies focused on estimating wind speed and direction, the potential of airborne systems to characterise atmospheric turbulence remains largely unexplored. Characterising turbulence includes measuring the turbulence intensity for each component, as well as the turbulence integral time and length scales.

AWE technology uses tethered flying devices, more simply labelled as 'kites', to harvest wind energy at altitudes beyond the reach of conventional wind turbines, where the wind is generally less variable and of higher mean speed. Compared to conventional wind turbines, AWES can substantially reduce material usage by replacing towers and rotors with tethered airborne devices, Cherubini et al. (2015) and Fagiano et al. (2022) provide comprehensive overviews of AWES. Various AWES concepts are being developed, ranging from rigid kites, to soft kites with ground generation or onboard generation. Figure 1 shows Kitemill's concept, which is the system considered for this research. That is a rigid kite operating in ground generation or *ground-gen* mode. For the ground-gen concept, wind energy is harvested by converting the pulling force of the kite using a drum generator on the ground station. To that end, the kite is operated in pumping cycles, alternating between two differentiated phases: production or reel-out phase, and return or reel-in phase (Van Der Vlugt et al., 2013). In the production phase, the kite is reeled out and flies in crosswind manoeuvres to maximize the tether tension transferred to the ground station. Such crosswind manoeuvres follow typically circular loops (resulting in a helical path when reeled out) or figure-of-eight loops, see Eijkelhof et al. (2026) for an in-depth comparison of flight patterns. For this paper circular loops are employed. Once the production phase ends, the kite is reeled back in at low tether tension to restore the system to its initial state and start the next cycle. As the return phase consumes a fraction of the energy generated in production phase, the technology provides a net positive cycle power. The length/duration of the production phase with respect to the return phase is a function of the net cycle power optimisation including constraints such as maximum tether length.

https://doi.org/10.5194/wes-2026-150
Preprint. Discussion started: 18 September 2026

Figure 1. Aerial component of Kitemill's KM1 system.

The paper is structured as follows. Section 2 presents the simulation framework for modelling the AWES and the atmospheric turbulence employed for this research. Following, Section 3 describes how the turbulence signal can be quantified from the kite's onboard sensors. Section 4 presents the main results of the paper, showing how to measure atmospheric turbulence through an AWES for both the return phase, Section 4.1 and the production phase, 4.2. Lastly, Section 5 concludes this study.

2 Simulation framework

The methodology and results presented in this paper have been obtained through the Universal Simulator for Airborne Wind Energy (UniSimAWE), Kitemill's in-house simulator. UniSimAWE is a Julia-based simulator environment for ground-gen rigid AWES, as shown in Figure 1. It is built around a six-degree-of-freedom (6-DOF) rigid-body model of the kite. The equations of motion are formulated through Newton's second law and Euler's moment equations, integrated using the stiff TRBDF2 ODE solver from the DifferentialEquations.jl library (Rackauckas and Nie, 2017). Simulation outputs for this work are recorded at a (tunable) sampling frequency of $f_s = 10\,\mathrm{Hz}$ in the North-East-Down (NED) reference frame, with the origin at the ground station.

The net forces and moments on the kite contain contributions from the aerodynamic, gravitational, and tether components. The aerodynamic model expresses the force and moment coefficients (C_D, C_Y, C_L, C_l, C_m, C_n) as polynomial functions of angle of attack, sideslip angle, and control surface deflections (ailerons, elevator, rudder, and flaps). Said polynomial functions are augmented with damping terms from the body-axis angular rates (p, q, r). The tether is modelled as a multi-node

https://doi.org/10.5194/wes-2026-150
Preprint. Discussion started: 18 September 2026

lumped-mass chain; each segment is treated as a spring-damper element with distributed gravity and aerodynamic drag acting on each segment. Flight control during the production looping phase is implemented through PID controllers governing attitude and reel-out, following the architecture proposed by Nguyen et al. (2026), complemented by a PID winch speed controller.

The atmospheric turbulence is modelled through the Mann model (Mann, 1994), a spectral method that represents the three-dimensional turbulent wind field as a homogeneous, anisotropic Gaussian random field. The model characterises the turbulence through three parameters:

- the length scale L_{MM} (m), the size of the energy-containing eddies, where the $_{\mathrm{MM}}$ subscript, standing for Mann model, is added to avoid confusion with other length scales.
- the energy dissipation rate $\alpha_{\mathrm{MM}}\varepsilon^{2/3}$ $(\mathrm{m}^{4/3}\mathrm{s}^{-2})$, scaling the overall turbulence intensity, where ε is the viscous dissipation rate of turbulent kinetic energy and α_{MM} is the Kolmogorov spectral constant as used in the Mann model[1].
- the anisotropy parameter Γ, controlling the distortion of the turbulence structure due to shear.

The 3D fields for the three velocity components (u', v', w') are referred to as "turbulence boxes" and are generated using the Hipersim tool, Dimitrov et al. (2024), an open-source Python implementation of the Mann model, Mann (1998). Figure 2 shows an example of a vertical section of a turbulence box for the streamwise turbulence field generated with Hipersim. The velocity field is discretised through 3D cells with a length, width, and height (Δx_{MM}, Δy_{MM}, Δz_{MM}). In the simulation, the three turbulence boxes (one per each component) are convected downstream with the streamwise mean wind speed; consequently, the kite senses a varying wind speed due to sampling different points (cells) in the box. Repeatability of simulations is ensured by the model by allowing to define a random seed, which can be fixed to regenerate an identical turbulence box.

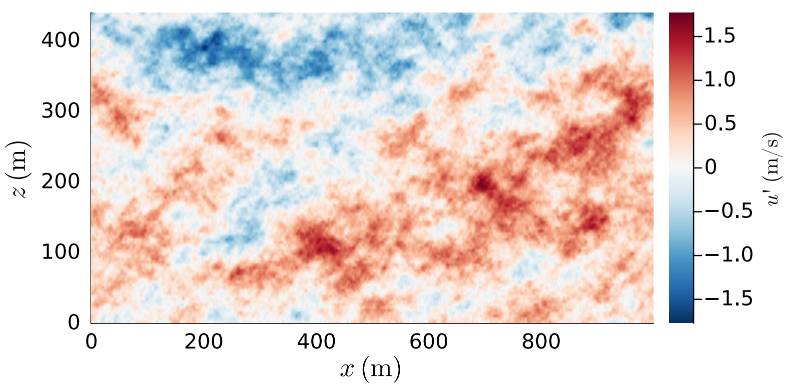

Figure 2. Example of a vertical cross-section of the streamwise turbulence component u' from a Mann model turbulence box (the reference frame is specific for the box.

[1]Note that α is also used to denote the angle of attack throughout this paper; the intended meaning is clear from context in each case.

https://doi.org/10.5194/wes-2026-150
Preprint. Discussion started: 18 September 2026

3 Computation of turbulence fluctuation from onboard sensors

While the results presented in this paper are obtained through the UniSimAWE simulation framework, the methodology is developed from quantities measurable by the kite's typically present onboard sensors, making it directly applicable to real AWES operation. The first step to obtain the turbulence fluctuations sensed by the kite is to measure the wind velocity vector. For any device flying through the atmosphere, there is a relationship between the following velocity vectors:

- the wind velocity $\boldsymbol{v_w} = [u, v, w]$
- the apparent wind velocity seen by the device $\boldsymbol{v_a}$
- the device (kite) velocity $\boldsymbol{v_k}$

As a result of the relative motion, the following equation is inferred:

$$\boldsymbol{v_a^n} = \boldsymbol{v_w^n} - \boldsymbol{v_k^n}, \tag{1}$$

where the ^{n} superscript denotes the NED reference frame. Note the distinction between the apparent wind velocity, $\boldsymbol{v_a}$, defined with Equation 1 and the relative kite velocity, $\boldsymbol{v_r}$ which is defined as

$$\boldsymbol{v_r^n} = -\boldsymbol{v_a^n} = \boldsymbol{v_k^n} - \boldsymbol{v_w^n}, \tag{2}$$

and represents the kite velocity relative to the wind. The airspeed, here denoted as V_a, is then the magnitude of the apparent wind velocity and of the relative kite velocity (as their magnitude are the same), $V_a = \|\boldsymbol{v_a}\| = \|\boldsymbol{v_r}\|$. Figure 3 shows the geometric velocity vector relationship for a kite flying in perfect crosswind, i.e. the kite velocity is normal to the wind.

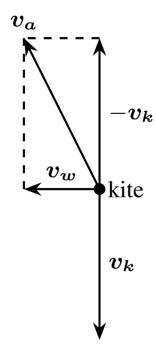

Figure 3. Velocity triangle for a kite flying in perfect crosswind, illustrating the relationship between kite velocity $\boldsymbol{v_k}$, wind velocity $\boldsymbol{v_w}$, and apparent wind velocity $\boldsymbol{v_a}$.

The relation given by Equation 1 can be employed to obtain the wind velocity vector from the kite velocity and apparent wind velocity. The kite velocity can be computed by numerically differentiating the kite's position, measured by the Global Navigation Satellite System (GNSS) sensor onboard. On the other hand, the relative kite velocity is derived from:

$$\boldsymbol{v_r^n} = R_b^n \cdot R_w^b \cdot [V_a, 0, 0]^\top, \tag{3}$$

https://doi.org/10.5194/wes-2026-150
Preprint. Discussion started: 18 September 2026

where the R_i^j is the rotation matrix from reference frame i to j. The frame b denotes the body frame and the w, the wind frame, as defined in Stengel (2022). A typically available sensor in the kite is the multi-hole probe, which measures the airspeed, V_a and the angle of attack α and sideslip angle β, inferred from the differential pressure readings between holes oriented in different directions. The angle of attack and sideslip allow us to construct the rotation matrix from wind frame to body frame, R_w^b. Lastly, the rotation matrix from body frame to NED frame, R_b^n can be constructed through the kite's attitude, i.e. the roll, pitch, and yaw angles, which can be obtained by combining the GNSS and the Inertial Navigation System (INS). With V_a, R_w^b, and R_b^n one can obtain the relative kite velocity $\boldsymbol{v_r^n}$ through Equation 3, which can be plugged into Equation 2 resuling on:

$$\boldsymbol{v_w^n} = \boldsymbol{v_k^n} - R_b^n \cdot R_w^b \cdot [V_a, 0, 0]^\top. \tag{4}$$

This methodology is employed in UniSimAWE assuming the parameters measurable by the onboard sensors are known, i.e. kite velocity, apparent wind velocity (airspeed, α, β) and kite attitude are perfectly known in the simulation. Such assumption disregards the noise of the sensors signal that would be present in real operation, as it is not in the scope of this paper. Figure 4 shows the streamwise component of the three vectors depicted in Figure 3 for a gliding flight path against the wind, equivalent to a return phase of an AWES pumping cycle operation (further described in Section 4), illustrating the relationship from Equation 1 in the streamwise direction ($v_{a,x} = u - v_{k,x}$).

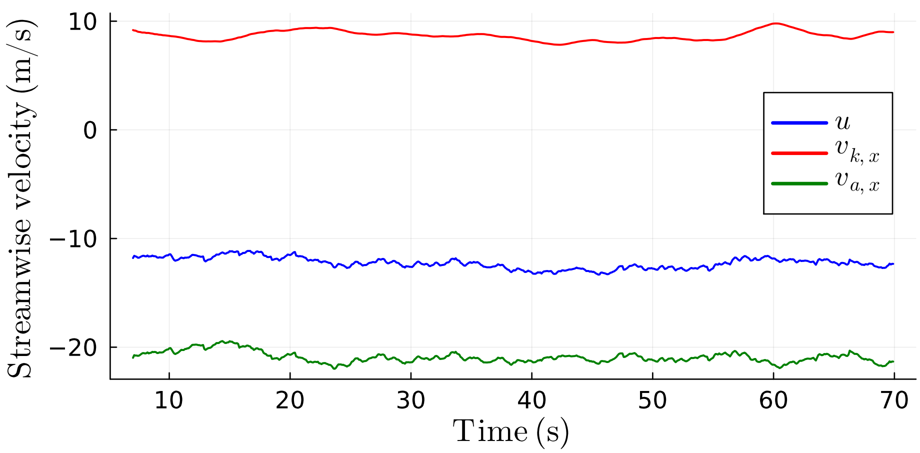

Figure 4. Streamwise component of $\boldsymbol{v_w^n}$, $\boldsymbol{v_k^n}$ and $\boldsymbol{v_a^n}$ obtained from simulation.

Once the wind velocity is obtained, the streamwise turbulence fluctuation u' is computed by subtracting the streamwise mean wind speed, U:

$$u' = u - U. \tag{5}$$

This is performed analogously for v' and w'; however, as the mean wind is aligned with the x direction, the mean lateral and vertical wind speed components are zero, giving $v' = v$ and $w' = w$. If shear is present, the mean wind speed varies with

https://doi.org/10.5194/wes-2026-150
Preprint. Discussion started: 18 September 2026

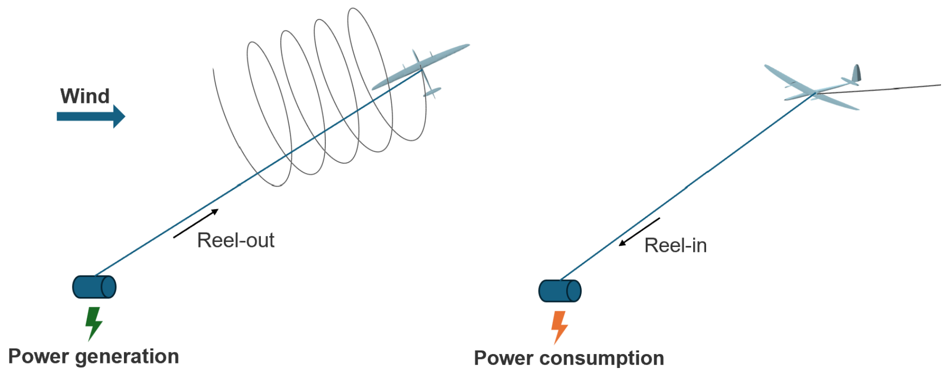

(a) Production phase. (b) Return phase.

Figure 5. Schematic illustration of the pumping cycle characteristic of the ground-gen AWES concept.

altitude, and subtracting a single constant U as in Equation 5 implicitly assumes this variation is negligible over the kite's operational altitude range. This assumption is valid for the simulations in this research as shear has not been considered, i.e. the wind velocity sensed by the kite is purely the addition of a mean wind speed, U, and the turbulence fluctuation given by the turbulence box. In real operation, the mean wind speed subtraction should account for shear if significant shear is present in the operational range.

4 Turbulence characterisation along the AWES pumping cycle

This section describes a methodology to obtain the turbulence characteristic parameters during the AWES pumping cycle, consisting of the production (reel-out) and return (reel-in) phases, as illustrated schematically in Figure 5.

The pumping cycle allows us to sample turbulence through two very distinct phases, reinforcing the potential of AWES as turbulence measurement devices, as different parameters are extractable from each phase. The distinction between these two phases is illustrated in Figures 6 and 7, containing key parameters characterising each particular phase. The different trajectories are shown through the kite position and velocity, where the production phase follows a helical path in the wind direction (towards negative x in this example), while the return phase glides back (towards positive x) to start the production phase again. Note that the airspeed and tether load are much higher for the production phase, as the kite flies in crosswind manoeuvre to maximise the pulling force, and thus the energy production. The angle of attack also differs among these two phases, as it is higher for the production phase, while the sideslip oscillates around 0 for both phases. The whole pumping cycle trajectory is shown in Figure 8 with a frozen state of the turbulence eddies as modelled by the Mann model, obtained from UniSimAWE. The duration of the production and return phases shown for this example are not optimised, thus they are not necessarily representative.

Given that the production and return phases follow completely different paths, the turbulence sampling strategy differs for each phase, thus they are explored individually in sections 4.1 and 4.2. The employed wind and atmospheric turbulence model

https://doi.org/10.5194/wes-2026-150
Preprint. Discussion started: 18 September 2026

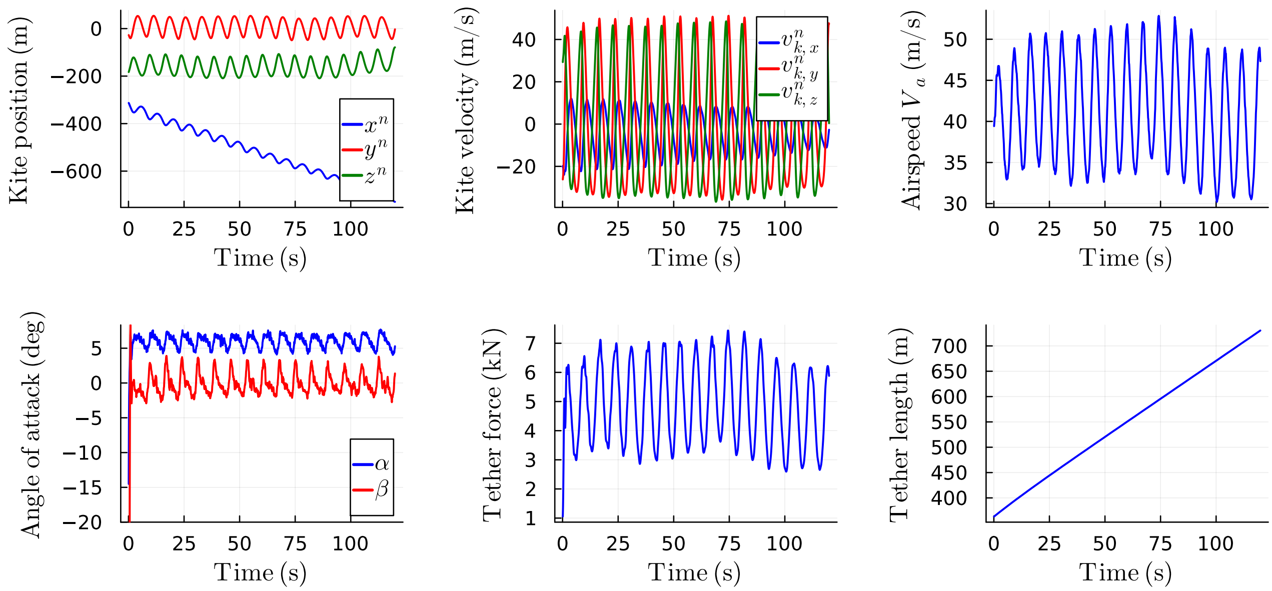

Figure 6. Time series of relevant variables during production phase obtained through UniSimAWE.

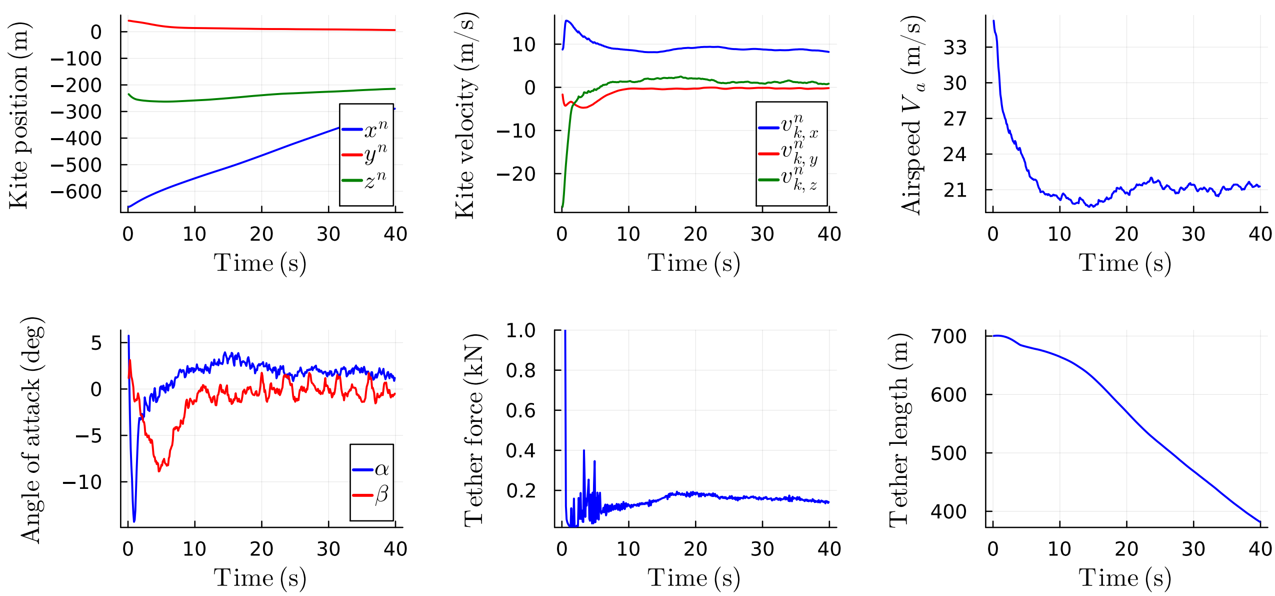

Figure 7. Time series of relevant variables during return phase obtained through UniSimAWE.

https://doi.org/10.5194/wes-2026-150
Preprint. Discussion started: 18 September 2026

for both phases is the same, allowing for comparison of turbulence parameters between the two phases. A mean wind speed $U = 12\,\text{m/s}$ has been employed, aligned with the x^{n} direction, pointing to negative x. The Mann model turbulence box used for the simulations in this paper has been constructed with the parameters shown in Table 1, unless stated otherwise.

Table 1. Mann model employed parameters.

Parameter	$\alpha\epsilon^{2/3}$ $(\text{m}^{4/3}\text{s}^{-2})$	L_{MM} (m)	Γ (-)	Δx_{MM} (m)	Δy_{MM} (m)	Δz_{MM} (m)
Value	0.011	100	3.0	1.0	4.0	4.0

Both the employed energy dissipation rate $\alpha_{\text{MM}}\epsilon^{2/3}$ and Mann model length scale L_{MM} are representative of Kitemill's test site at Lista, Norway; they can be obtained from the site's 9-month dataset Lidar measurements through the expressions

$$L_{\text{MM}} = \frac{\sigma_u}{\partial U/\partial z} \tag{6}$$

$$\alpha_{\text{MM}}\epsilon^{2/3} = 0.57\sigma_u^2 L_{\text{MM}}^{-2/3} \tag{7}$$

derived by Kelly (2018), also used with the IEC 61400-1 standard for typical wind turbines (International Electrotechnical Commission, 2020). The anisotropy parameter has been estimated as $\Gamma = 3.0$, per the (neutral) conditions in this example at Kitemill's site, following from Kelly (2025, Appendix A), consistent also with de Mare and Mann (2016).

4.1 Turbulence characterisation along the return phase

In the return phase, the kite glides back towards the initial production position while the tether is reeled in to start the production phase again. Note that Figure 8 depicts the return phase in dark green, including the transitions from and to the production phase, however, for this analysis the transitions are disregarded. In this phase, the kite mainly translates in the streamwise direction, against the wind, while losing altitude ($v_{k,z}$ is slightly positive in NED) and keeping a constant lateral component.

Employing the methodology described in Section 3 the turbulence fluctuations u', v' and w' are obtained as a time series along the return phase, shown in Figure 9. The time series can be employed to compute the standard deviation σ_u, thus leading to the turbulence intensity sensed by the kite, I_u when normalised with the mean wind speed, providing a relevant turbulence parameter,

$$I_u = \frac{\sigma_u}{U}. \tag{8}$$

The turbulence intensities for this case are $I_u = 4.3\%$, $I_v = 3.2\%$, and $I_w = 2.8\%$, consistent with the turbulence conditions prescribed by the Mann model parameters in Table 1. Inverting Equation 7 results in $\sigma_u = 0.64\,\text{m/s}$, with the employed dissipation rate and length scale, from which $I_u = \sigma_u/U = 5.3\%$ for $U = 12\,\text{m/s}$, in reasonable agreement with the obtained value from the time series.

https://doi.org/10.5194/wes-2026-150
Preprint. Discussion started: 18 September 2026

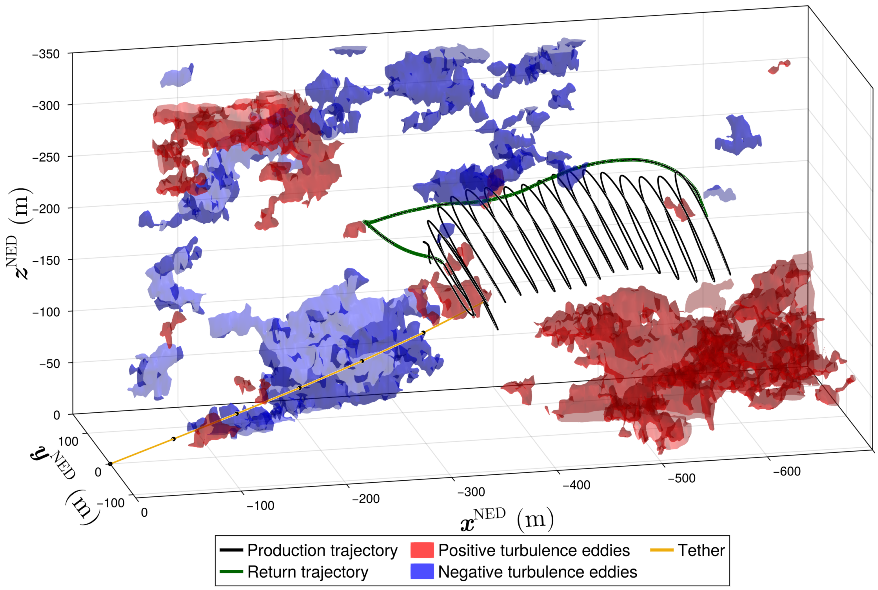

Figure 8. 3D illustration of the AWES typical trajectory during the pumping cycle, with frozen state of the turbulence eddies and the tether segments.

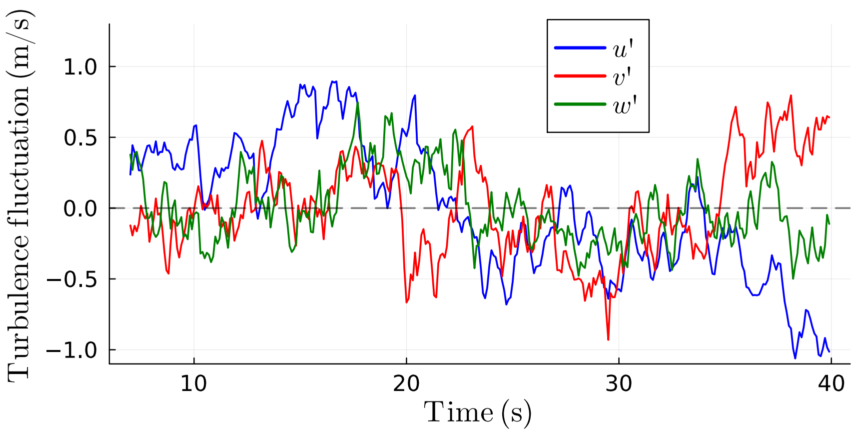

Figure 9. Turbulence fluctuations u', v', and w' as a time series during the return phase.

In order to obtain the integral time scale $\mathcal{T}_u$, the autocorrelation function (ACF), $\rho(\tau)$, must be computed from the uniformly sampled turbulence time series (its Δt is constant). As the time lag τ increases, successive samples become less correlated and $\rho(\tau)$ decays towards zero. The integral timescale $\mathcal{T}_u$ characterises both this rate of decay and the overall "memory" time of the

https://doi.org/10.5194/wes-2026-150
Preprint. Discussion started: 18 September 2026

signal, defined as the area below the ACF:

$$\mathcal{T}_u \equiv \int_0^\infty \rho(\tau) d\tau. \tag{9}$$

Practically, this might be seen as the area from $\tau = 0$ to the first intersection of $\rho = 0$, since $\rho(\tau)$ can often 'wiggle' above and below zero for large τ. For robust calculation insensitive to such low-correlation oscillations, we follow the common turbulence methodology of fitting the $\rho(\tau)$ with an exponential curve, thus disregarding noise for large time lags:

$$\rho_u(\tau) \approx e^{-\tau/\mathcal{T}_u}. \tag{10}$$

Consequently we have $\int_0^\infty e^{-\tau/\mathcal{T}_u} d\tau = \mathcal{T}_u$, giving the timescale directly as the fitted decay constant. Large $\mathcal{T}_u$ indicate slowly decorrelating turbulence (large structures), while small $\mathcal{T}_u$ indicate rapidly decorrelating (smaller-scale) turbulence. Figure 10 shows $\{\mathcal{T}_u, \mathcal{T}_v, \mathcal{T}_w\}$ for $\{u', v', w'\}$ with the respective exponential fits to $\{\rho_u, \rho_v, \rho_w\}$; a logarithmic y-axis is used such that a linear ACF corresponds to a pure exponential function, showing that the ACF exponentially decays for small time lags. Note that a logarithmic y-axis is useful for identifying exponential behaviour, but it distorts visual area because the axis compresses large values of ρ and expands small ones. The integral time scale of the streamwise fluctuations is larger than the lateral component, which is larger than the vertical component time scales, with $\mathcal{T}_u > \mathcal{T}_v > \mathcal{T}_w$. This is consistent with shear production of u' driving turbulence; the Mann (1994) model's shear distortion generates turbulence where the streamwise dimensions are larger than its lateral dimensions, which are larger than its vertical dimensions, with the relative sizes controlled by the model's anisotropy parameter, Γ.

https://doi.org/10.5194/wes-2026-150
Preprint. Discussion started: 18 September 2026

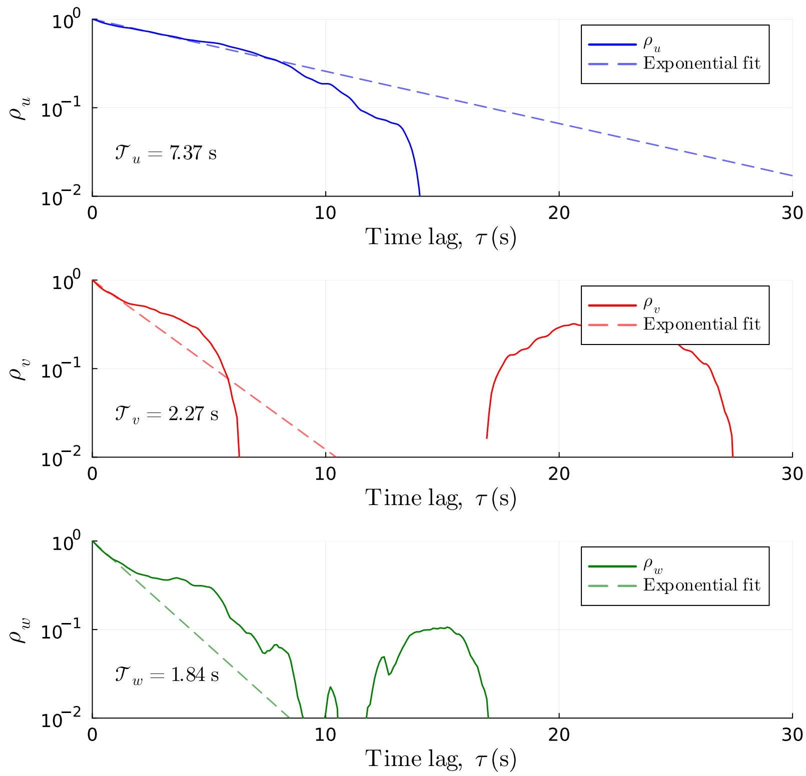

Figure 10. Autocorrelation function of turbulence fluctuations u', v', and w' as a function of time lag τ, with the exponential fits and the resulting integral time scales $\mathcal{T}_u$, $\mathcal{T}_v$, $\mathcal{T}_w$.

Note from Figure 10 that the v- and w-scales could be larger than diagnosed since there is another "straight" part at the initial autocorrelation decay. However, the exponential fit is a weighted fit where more relevance is given to the initial time lags through a $w_i = 1/i$ weighting, where i is the index of the ACF point. Such weighting ensures the fitted exponential characterises the initial ACF decay. The time scales obtained through the exponential fit have been ensured to be within 10% at most of the time scales that would be obtained with the actual $\rho(\tau)$. $w_i = 1/i$,

The integral length scales can be similarly obtained by using the turbulence fluctuation x series instead of the time series, where x is relative to the flow field. Note that, unlike the time series, the spatial series is non-uniform since the distance travelled between consecutive samples of constant Δt varies with the non-constant kite speed. A uniform spatial grid is required for the ACF computation; hence the turbulence fluctuations are resampled into an equidistant x grid through a linear interpolation. The ACF is then computed on $u'(x)$, $v'(x)$ and $w'(x)$, providing the memory of the turbulent signal as the x component relative to the flow field increases, shown in Figure 11, as well as the integral length scales obtained by fitting an exponential curve.

https://doi.org/10.5194/wes-2026-150
Preprint. Discussion started: 18 September 2026

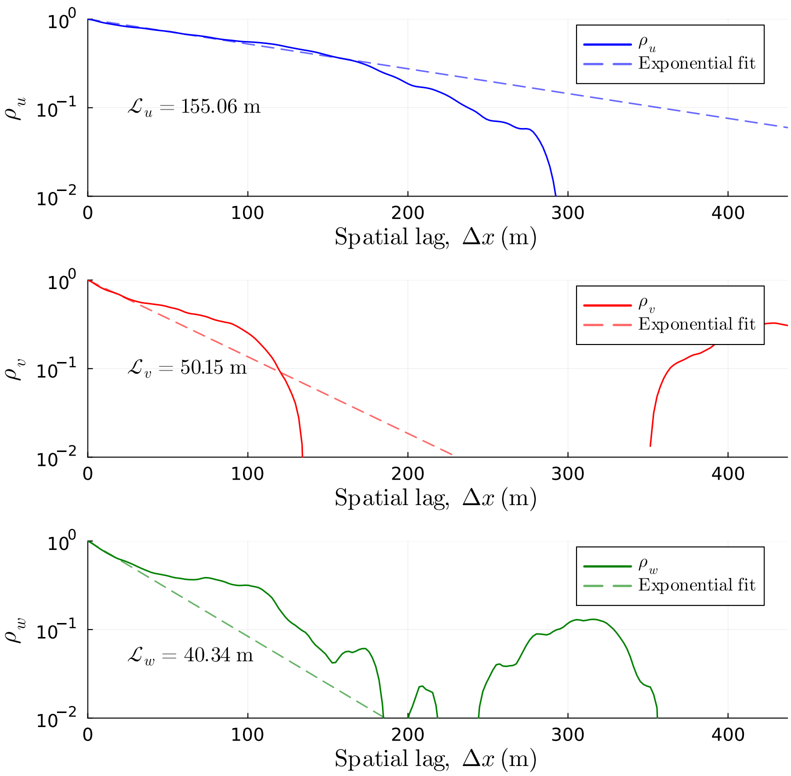

Figure 11. Autocorrelation function of turbulence fluctuations u', v', and w' as a function of spatial lag Δx relative to the flow field, with exponential fits and the resulting integral length scales $\mathcal{L}_u$, $\mathcal{L}_v$, $\mathcal{L}_w$.

With the integral time and length scales, the Taylor's frozen turbulence hypothesis from Taylor (1937), can be validated. This hypothesis states that turbulent eddies move downstream with the mean wind speed and assumes the structures remain mostly unchanged as they propagate (Taylor, 1938). Thus, measured time series can be interpreted as spatial signal, with the conversion between temporal and spatial domain given by the mean streamwise relative kite speed, $\bar{v}_{r,x}$ (or U for a conventional fixed-point sensor). Such a hypothesis, however, requires the sampling to be only in the streamwise direction, which is not exactly the case for the return phase trajectory. To validate if the hypothesis holds for such sampling strategy, the ratio of integral length scale to integral time scale is computed, which should result in the mean streamwise relative kite speed if Taylor's hypothesis holds. The ratio $\mathcal{L}/\mathcal{T}$ for the three components are shown in Table 2 with the comparison to the mean streamwise relative kite speed.

The three ratios $\mathcal{L}/\mathcal{T}$ for the u, v, and w components all lie within 6% of the mean streamwise relative kite speed $\bar{v}_{r,x} = 20.91\,\text{m/s}$ (this value comes from $U = 12\,\text{m/s}$ and $\bar{v}_{k,x} \approx 9\,\text{m/s}$, giving roughly 21m/s), as shown in Table 2. The discrepancy arises from the kite's trajectory not being perfectly aligned with the streamwise direction; instead it has a non-negligible displacement in the y and z directions, so consecutive samples are not strictly separated in the streamwise direction as Tay-

https://doi.org/10.5194/wes-2026-150
Preprint. Discussion started: 18 September 2026

Table 2. Integral length and time scales for the three turbulence components during the return phase, and their ratio compared to the mean streamwise relative kite speed $\bar{v}_{r,x} = 20.91$.

Component	$\mathcal{L}$ (m)	$\mathcal{T}$ (s)	$\mathcal{L}/\mathcal{T}$ (m/s)	Relative deviation from $\bar{v}_{r,x}$ (%)
u	155.06	7.37	21.04	0.64
v	50.15	2.27	22.10	5.71
w	40.34	1.84	21.97	5.09

lor's hypothesis assumes. However, since the dominant motion is streamwise, the deviation remains small and the Taylor's hypothesis can be considered to hold for this sampling strategy.

Such ratio has been computed for various simulations with a varying Mann model length scale, $L_{\mathrm{MM}} = [10, 50, 100, 150, 200]$ m such that different eddies sizes are tested (each case with different random seeds to ensure different turbulence boxes). The integral length and time scales results are shown for the three components u, v, and w in Figure 12. A linear regression is fit to the integral scales for each component, where the slopes for the three components result in the relative wind speeds (20.4 m/s, 21.0 m/s and 21.3 m/s) close to the actual streamwise relative wind speed, confirming the validation of Taylor' shypothesis. It is inferred that the Taylor's hypothesis holds well when sampling the turbulence signal in the return phase, meaning that an estimate of the integral length scales can be obtained directly from the integral time scales through the relative kite speed, as is often done for "conventional" fixed-point measurement devices.

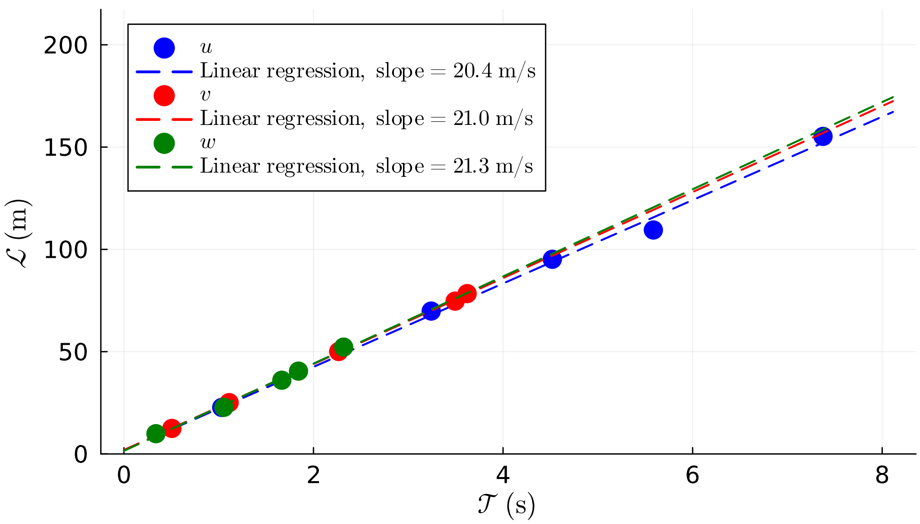

Figure 12. Integral length scale $\mathcal{L}$ vs. integral time scale $\mathcal{T}$ for the three turbulence components for different Mann model length scales with their respective linear regressions.

https://doi.org/10.5194/wes-2026-150
Preprint. Discussion started: 18 September 2026

The variance, σ^2 of the turbulence signal can be obtained through the frequency-domain power spectral density (PSD), $S(f)$, with

$$\sigma^2 = \int_{-\infty}^{\infty} S(f)\mathrm{d}f = \int_{-\infty}^{\infty} fS(f)\mathrm{d}(\ln f). \tag{11}$$

The PSD of the turbulence fluctuations is computed via the discrete Fourier transform (DFT). For the frequency-domain PSD, the DFT is applied to the turbulence fluctuation time series $u'(n\Delta t)$, $n = 0, \ldots, N-1$, sampled at a uniform interval Δt with sampling frequency $f_s = 1/\Delta t = 10\,\mathrm{Hz}$:

$$\hat{u}(f) = \sum_{n=0}^{N-1} u'(n\Delta t)e^{-2\pi i f n\Delta t}. \tag{12}$$

The one-sided PSD is then obtained as

$$S_{uu}(f) = \frac{2|\hat{u}(f)|^2}{Nf_s}, \quad f > 0, \tag{13}$$

with units m^2s^{-1}, where the factor of 2 in the $S_{uu}(f)$ equation accounts for the negative-frequency energy, adding it to the positive-frequency axis. The normalisation with Nf_s ensures that integrating the PSD over all frequencies recovers the total variance of the signal. Since the raw spectra is noisy, $S(f)$ is smoothed by logarithmic binning with 12 bins per decade, averaging S within each bin (shown in Appendix A).

Figure 13 shows the spectral distribution of variance through the pre-multiplied PSD for each component, i.e. $f \cdot S_{\beta\beta}$, for $\beta = \{1,2,3\}$, where the $S(f)$ is the smoothed signal.[2] Note that the area under each curve in the figure equals σ_β^2 (Equation 11), while the spectral distribution allows us to infer at what frequencies there is a more variance. It is shown that the variance is concentrated at low frequencies, consistent with the energy-containing eddies. The streamwise variance peak is at lower frequency than the lateral and vertical ones, depicting the larger eddies in the streamwise component.

[2]Following typical turbulence convention and Einstein notation use, repeated Greek indices indicate separate turbulence components.

https://doi.org/10.5194/wes-2026-150
Preprint. Discussion started: 18 September 2026

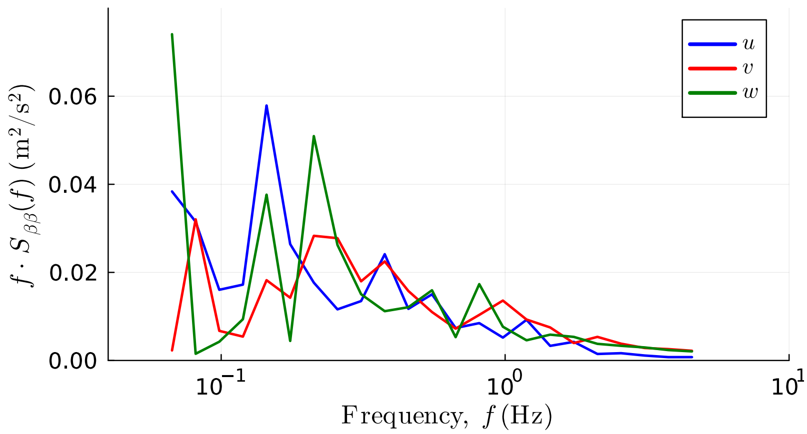

Figure 13. Pre-multiplied frequency-domain PSD $fS_{uu}(f)$, $fS_{vv}(f)$, and $fS_{ww}(f)$ of turbulence fluctuations during the return phase, showing the variance spectral distribution.

The frequency-domain PSD can be employed together with the wavenumber-domain PSD, $\Phi(k_1)$ to further validate the Taylor's hypothesis for the return phase. From Taylor's hypothesis, the two quantities should be related through the mean streamwise relative kite speed, $\bar{v}_{r,x}$, with

$$\frac{\Phi_{\beta\beta}(k_1)}{S_{\beta\beta}(f)} = \bar{v}_{r,x}/(2\pi), \tag{14}$$

where the 2π term is added due to the cycles to radians conversion. The wavenumber-PSD, $\Phi(k_1)$ is obtained analogously from the uniformly resampled spatial frequency $u'(m\Delta x)$ with spatial sampling rate $\kappa_s = 1/\Delta x$ (cycles m^{-1}), which is converted to radial wavenumber with $k_1 = 2\pi\kappa_s$ (rad m^{-1}), giving

$$\Phi_{uu}(k_1) = \frac{2}{2\pi}\frac{|\hat{u}(k_1)|^2}{N\kappa_s}, \quad k_1 > 0, \tag{15}$$

with units $\mathrm{m^3\,s^{-2}}$.

The ratio from Equation 14 is evaluated by converting the wavenumber axis to frequency via $f = k_1\bar{v}_{r,x}/(2\pi)$, so that both PSD's are expressed as functions of the same variable, f. Figure 14 shows the ratio for the three components u, v and w computed with the smoothed signal, the ratios are shown to be close to the expected value of $\bar{v}_{r,x}/(2\pi)$, though not exactly. Similar to the previous Taylor's hypothesis validation through the integral scales ratio, $\mathcal{L}/\mathcal{T}$, the following sources of deviation are identified. First, the kite follows a trajectory with a non-negligible displacement in the y and z directions, so the sampled spatial series does not align perfectly with the streamwise axis of the turbulence field. Second, the wavenumber-PSD is computed from a spatially resampled series obtained by linear interpolation into a uniform Δx grid, which introduces a small interpolation error. A decay of the ratio from the expected value is observed for higher frequencies, around $f > 3Hz$. This is attributed to the linear interpolation used to obtain the uniform spatial grid, which acts as a low-pass filter in the spatial domain, thus reducing Φ at high wavenumbers (this is investigated in detail by Wyngaard and Clifford (1977) following the

https://doi.org/10.5194/wes-2026-150
Preprint. Discussion started: 18 September 2026

eawe european academy of wind energy
Open Access WIND ENERGY SCIENCE DISCUSSIONS

original theory of Lumley (1965), and for cross-wind 'damping' one can see e.g. Tong and Wyngaard (1996)). This validation shows that the wavenumber-domain PSD can be estimated from the frequency-domain PSD through the streamwise relative kite speed with accuracy degrading at high frequencies due to the effect identified above.

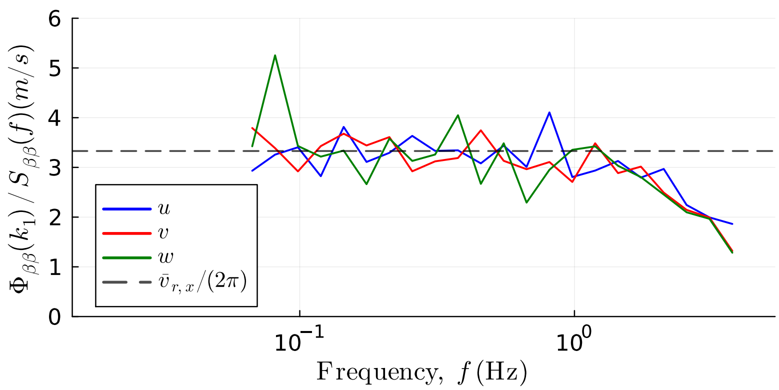

Figure 14. Ratio $\Phi_{\beta\beta}(k_1)/S_{\beta\beta}(f)$ for the three turbulence components during the return phase, compared to the expected value $\bar{v}_{r,x}/(2\pi)$ (dashed line) according to Taylor's hypothesis.

270 ### 4.2 Turbulence characterisation along the production phase

The production or reel-out phase of the pumping cycle is now evaluated to quantify turbulence. Recall that in this phase, the kite loops in a helical path, see Figure 8. The turbulence intensity for the three components are similarly computed through the turbulence fluctuations time series, resulting in $I_u = 3.6\%$, $I_v = 4.0\%$, and $I_w = 3.1\%$, consistent with the values obtained during the return phase. The agreement is expected, as the employed turbulence box is the same and the turbulence intensity is a property of the turbulence field amplitude, thus independent of the sampling strategy. The reason for the small discrepancy is that the two phases sample different spatial regions of the turbulence box.

For the production phase, the Taylor's hypothesis cannot be employed due to the dominant crosswind motion in the looping trajectory. The kite slices through eddies lateral and vertically, rather than sampling them along the streamwise direction, such that a temporal lag no longer maps to a streamwise spatial displacement. Consequently, one cannot invoke the Taylor's hypothesis to convert a time or frequency domain variable to a spatial or wavenumber domain variable through the mean streamwise relative kite speed. The effect of the crosswind component in the sampling strategy "disabling" the Taylor's hypothesis is further described in Appendix B.

The autocorrelation function is computed again with the turbulence fluctuation time series, $u'(t)$, $v'(t)$, and $w'(t)$, leading to the integral time scale by fitting an exponential, shown in Figure 15. The sampling strategy must be taken into account to interpret the obtained time scale. Due to the dominant crosswind component in the production trajectory, i.e. $|v_{k,yz}| >> |v_{k,x}|$, the kite is mostly slicing the eddies in the y-z plane. Therefore, the memory of the turbulent signal decays very rapidly, leading to very low time scales, in the order of $\sim 1\,\mathrm{s}$. These time scales are a measure of the memory time of the turbulence signal

https://doi.org/10.5194/wes-2026-150
Preprint. Discussion started: 18 September 2026

in the crosswind direction, thus referred to as $\mathcal{T}_{u,yz}$, $\mathcal{T}_{v,yz}$, and $\mathcal{T}_{w,yz}$, with the added $_{yz}$ subindex referring to the crosswind component. Note that the kite's trajectory does not lie strictly in the y-z plane due to the reel-out speed, however the adopted
290 assumption is that the streamwise component is small compared to the crosswind component. The corresponding integral length scales can be derived through the crosswind kite speed, $v_{k,yz}$ with:

$$\begin{aligned}
\mathcal{L}_{u,yz} &= v_{k,yz}\,\mathcal{T}_{u,yz}, \\
\mathcal{L}_{v,yz} &= v_{k,yz}\,\mathcal{T}_{v,yz}, \\
\mathcal{L}_{w,yz} &= v_{k,yz}\,\mathcal{T}_{w,yz}.
\end{aligned} \tag{16}$$

Note that this conversion (Equation 16) is analogous to Taylor's frozen turbulence hypothesis applied in the crosswind direction, where the kite's crosswind speed $v_{k,yz}$ replaces the mean streamwise relative kite speed. Unlike the classical hypothesis,
295 this relies on the kite's motion rather than flow advection, but a frozen-eddy assumption is still implied. These length scales are a measure of the size of the eddies in the crosswind direction, a quantity inaccessible to conventional measurement techniques, therefore highlighting the potential of AWES as a turbulence sensing device.

https://doi.org/10.5194/wes-2026-150
Preprint. Discussion started: 18 September 2026

eawe european academy of wind energy
Open Access WIND ENERGY SCIENCE DISCUSSIONS

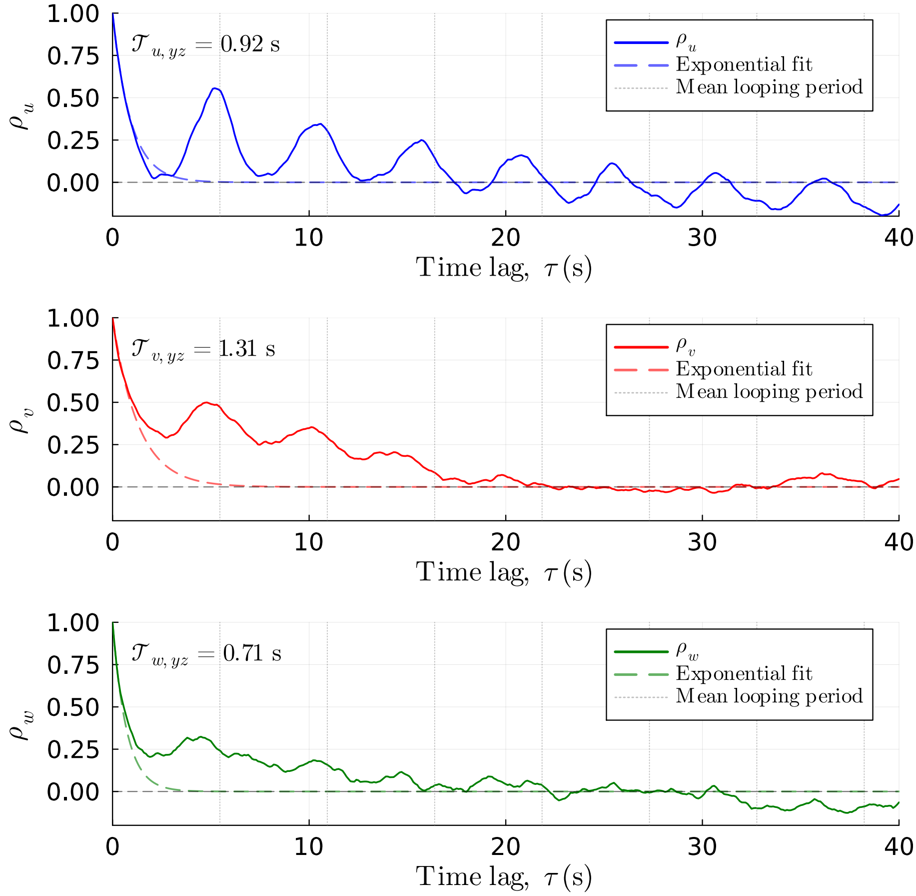

Figure 15. Autocorrelation function of turbulence fluctuations u', v', and w' during the production phase with the crosswind integral time scales $\mathcal{T}u,yz$, $\mathcal{T}v,yz$, $\mathcal{T}_{w,yz}$ obtained from the exponential fit to the ACF decay.

The function $\rho(\tau)$ is plotted in Figure 15 with a linear y axis instead of logarithmic to better visualize the oscillatory behaviour of the ACF. It shows that peaks occur periodically near the mean looping period (the mean is employed since the looping period varies along the production phase), and the height of such peaks progressively decays. These peaks in the ACF illustrate that the turbulence signal correlates after each full loop, meaning that the kite tends to sense the "same" turbulence eddy after a full loop. That occurs since the same region in the y-z plane is sampled after a looping period. Hence, the decay of the ACF peaks is a measure of the turbulence eddy scale in the streamwise direction. The peaks are more evident and lasting in the streamwise component of the turbulence, u', than in the lateral and vertical directions, which is consistent with the smaller integral time scales in those directions obtained from the return phase trajectory in Section 4.1.

By fitting an exponential function to the decay of peaks of the streamwise ACF, instead of the original ACF, the integral time scale in the streamwise direction can be obtained. Figure 16 depicts the exponential fit and the resulting integral time scale

https://doi.org/10.5194/wes-2026-150
Preprint. Discussion started: 18 September 2026

$\mathcal{T}_{u,x}$, from where it is shown that an exponential function fits the ACF peaks decay accurately. The fit is again obtained by weighting the peaks by $w_i = 1/i$, where i is the index of the peak, thus prioritising the earlier, more reliable peaks (note that the later peaks do not coincide with the looping periods). The corresponding time scale for the lateral and vertical direction are not computed as the peaks for those directions are not as prominent, meaning that the v' and w' eddies are not large enough in the streamwise direction for the kite to sense them after multiple loops. However, the same procedure would be applicable. An integral time scale of $\mathcal{T}_{u,x} = 9.96\,\mathrm{s}$ has been obtained, which is in the same order of magnitude as the $\mathcal{T}_{u,x} = 7.37\,\mathrm{s}$ obtained in with the return phase sampling. As the same turbulence box has been used for both cases, a similar value would be expected for $\mathcal{T}_{u,x}$. Such discrepancies, however, arise from the two phases sampling different spatial regions of the turbulence box, and hence different eddies, as well as from the mentioned assumptions introduced in each approach. Thus, the difference in the obtained $\mathcal{T}_{u,x}$ with the two sampling strategies is within an expected range.

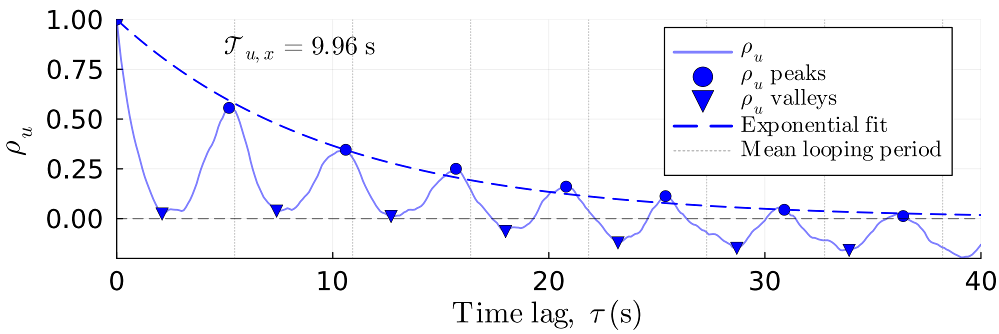

Figure 16. Autocorrelation function of streamwise turbulence fluctuation u' during the production phase with exponential fit to the ACF peaks, yielding the streamwise integral time scale $\mathcal{T}_{u,x}$.

Similarly to the ACF peaks, Figure 16 shows the respective valleys in the ACF, which illustrate that the turbulence signal on opposite sides of the loop (half looping period) is poorly correlated. Hence, another time scale can be derived that measures the decay of anti-correlation between opposite sides of the loop; such parameter is theoretically relatable to the spatial cross-covariance, although that is not in the scope of this work. This newly introduced time scale is not relevant to characterise the turbulence field itself, but to characterise how turbulence eddies interact with the AWES operation during looping. An example of a potential application of this parameter would be real-time active control of the AWES during looping. To derive this time scale, the difference of ACF is computed for each peak-valley pair:

$$\Delta\rho_u = \rho_{u,peak} - \rho_{u,valley}. \tag{17}$$

An exponential function is fit to the $\Delta\rho_u$ values, which are artificially placed at the same time lag τ as the ACF peaks, as shown in Figure 17.

https://doi.org/10.5194/wes-2026-150
Preprint. Discussion started: 18 September 2026

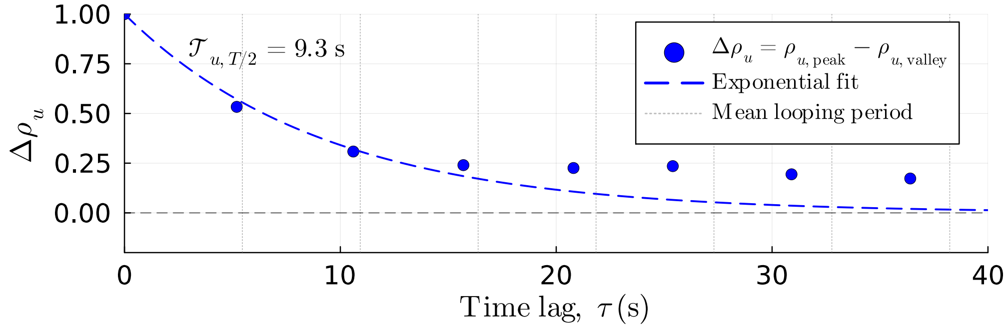

Figure 17. Autocorrelation function peak-valley difference $\Delta\rho_u$ with exponential fit, resulting in the half-period integral time scale $\mathcal{T}_{u,T/2}$ characterizing the decorrelation between opposite sides of the production loop.

The exponential fit shows that the $\Delta\rho_u$ points fit an exponential function well for the first points, the most relevant for the exponential fit as they have a higher weight in the fitting. The resulting time scale is referred to as the half-period integral time scale, $\mathcal{T}_{u,T/2}$, where the $_{T/2}$ subscript stands for half looping period, i.e. opposite sides of the loop. In this case, the $\mathcal{T}_{u,T/2}$ results on a similar value as $\mathcal{T}_{u,x}$ since the ACF valleys lie very close to 0, however, that is not always the case, as it depends on the eddies location and size with respect to the AWES helical path. An example of that is illustrated in Figure 18, showing the ACF for a simulation using a turbulence box with the same parameters as in the previous case (Table 1) but with a different random seed. It shows that the difference of correlation between opposite sides of the loop (peaks and valleys) is smaller meaning that there is a certain correlation between opposite sides, such behaviour occurs when the same turbulence eddy includes the whole production trajectory, i.e. opposite sided will show a certain correlation. The integral time scales for this case are $\mathcal{T}_{u,x} = 12.77\,\text{s}$ and $\mathcal{T}_{u,T/2} = 6.67\,\text{s}$ (not shown in the plot), illustrating a turbulence case with different $\mathcal{T}_{u,x}$ and $\mathcal{T}_{u,T/2}$.

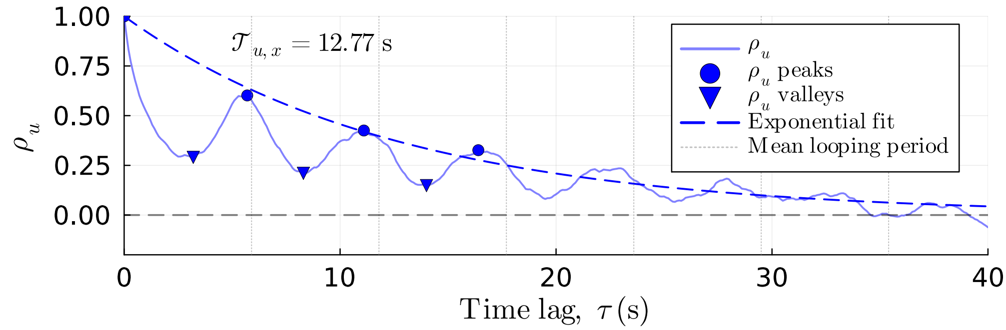

Figure 18. Autocorrelation function of streamwise turbulence fluctuation u' during the production phase for a different turbulence box with the exponential fit to the ACF peaks, yielding the streamwise integral time scale $\mathcal{T}_{u,x}$.

https://doi.org/10.5194/wes-2026-150
Preprint. Discussion started: 18 September 2026

WIND ENERGY SCIENCE DISCUSSIONS

The effect of the turbulence length scale on these newly defined parameters is shown by simulating a case where the Mann model length scale is reduced to $L_{\mathrm{MM}} = 10\,\mathrm{m}$, thus the turbulence eddies are significantly smaller in this case[3]. Note that such smaller length scale does occur relatively frequently, in particular for offshore flow, as shown in Kelly (2018) (Figs.5-6). The effect of reducing the eddies size is clearly shown by the ACF of the streamwise turbulence component and the resulting time scales $\mathcal{T}_{u,yz}$ and $\mathcal{T}_{u,x}$, shown in Figure 19. These time scales are significantly lower with respect to the original case ($L_{\mathrm{MM}} = 100\,\mathrm{m}$) as the ACF decays much faster, showing a very short time scale in the crosswind direction, $\mathcal{T}_{u,yz} = 0.25\,\mathrm{s}$ as well as in the streamwise direction obtained with the ACF peaks, $\mathcal{T}_{u,x} = 3.61\,\mathrm{s}$. The peaks are shown to fade after 2 loops mixing with the ACF noise, indicating that the streamwise turbulence is fully decorrelated on that timescale.

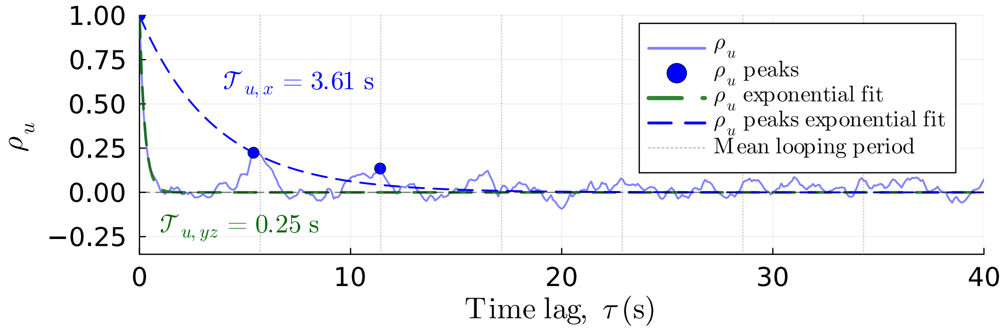

Figure 19. Autocorrelation function of streamwise turbulence fluctuation u' during the production phase for $L_{\mathrm{MM}} = 10\mathrm{m}$, showing significantly reduced integral time scales $\mathcal{T}_{u,yz}$ and $\mathcal{T}_{u,x}$ due to smaller turbulence eddies.

The spectrum of the turbulent velocity components are shown in Figure 20 through the pre-multiplied $f \cdot S_{\beta\beta}$, for $\beta = \{1,2,3\}$. The variance of the streamwise turbulence signal shows a clear peak at the looping frequency, illustrating that the kite's helical sampling path introduces a periodic component into the measured spectra. The peak is less pronounced for the lateral and vertical components, in agreement with the fewer and less evident peaks in their respective ACF curves. Such peaks, however, show that an additional step would be required to measure the turbulence spectra through an AWES during the production phase. Such effect is similarly shown in Petersen et al. (1995), where the wind speed spectra as seen from a point on a rotating blade of a conventional wind turbine depicts an analogous peak at the rotation frequency, due to the periodic sampling strategy.

[3]Such conditions have taken place at Kitemill's site in Lista, Norway on March 15^{th}, 2025 at 03:40.

https://doi.org/10.5194/wes-2026-150
Preprint. Discussion started: 18 September 2026

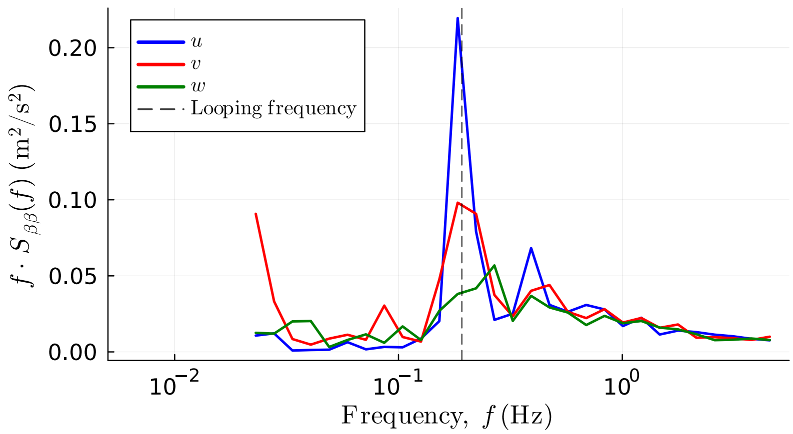

Figure 20. Pre-multiplied PSD, $f \cdot S_{\beta\beta}(f)$, of apparent component fluctuations during the production phase, showing the spectral distribution of variance.

5 Conclusions

This work demonstrates that an Airborne Wind Energy System (AWES) can serve as an effective atmospheric turbulence sensor. It provides turbulence parameters at heights that are not usually available for conventional fixed-point measurement devices, and with selectable resolutions much finer than those afforded by an individual commercial remote-sensing device. The turbulence fluctuations are derived from quantities measurable by the kite's onboard sensors: kite velocity and orientation (GNSS & INS) and apparent velocity (multi-hole probe), which are assumed to be known within the simulation framework here. These quantities lead to the wind velocity vector; subsequently subtracting the mean wind velocity then gives the turbulence fluctuations for each component.

The two main phases of the AWES pumping cycle for a ground-generation system, i.e., return and production phases, have been evaluated to explore the turbulence parameters that can be obtained. The turbulence intensity has been recovered for both phases, which is basically independent of the sampling strategy. Note that the turbulence intensity reflects the spatio-temporally integrated amplitude of the turbulence field rather than its spatial structure, and averaging over a large number of integral time and length scales supports such independence regarding the convergence of statistics. Since both phases have sampled the same synthesized velocity field, the variance is preserved regardless of the flight path. Beyond turbulence intensity, the two phases offer complementary information on the turbulence structures.

During the return phase, where the kite is retracted towards the ground station and follows a near-streamwise path, the integral time scales for the three turbulence components have been obtained through the temporal autocorrelation function of the turbulence signal. Similarly, the length scales have been obtained employing the turbulence fluctuations x series (instead of the time series) using the position of the kite relative to the flow field. The Taylor's frozen turbulence hypothesis has been shown to hold well for this near-streamwise sampling trajectory, as confirmed by the ratio of integral length and time scales ($\mathcal{L}/\mathcal{T}$),

https://doi.org/10.5194/wes-2026-150
Preprint. Discussion started: 18 September 2026

as well as the ratio of wavenumber-domain PSD to frequency-domain PSD (Φ/S). From both cases, the mean streamwise relative kite velocity component has been recovered, within a 6% accuracy for the $\mathcal{L}/\mathcal{T}$ case, confirming applicability of Taylor's hypothesis. Moreover, $\mathcal{L}/\mathcal{T}$ has been further shown to be consistent for an ensemble of turbulence simulations across a range of Mann-model length scales (L_{MM} from 10–200 m), with Taylor's hypothesis applicable independent of L_{MM}. Hence, for the turbulence sampled in the return phase, the direct conversion between time and length scales using the mean relative wind speed, analogous to conventional fixed-point sensors (or forward-looking nacelle lidar), can be employed. The turbulence spectra has also been shown to be obtainable through the return phase sampling.

For the AWES production phase, the sampling strategy to quantify turbulence is a helical trajectory, resulting in a novel approach for turbulence sensing. Due to the dominant crosswind motion in this phase, Taylor's hypothesis cannot be invoked to convert time scales to length scales (further explored in Appendix B). The crosswind looping trajectory allows one to obtain the integral time scales in the crosswind (y-z) plane, $\{\mathcal{T}_{u,yz}, \mathcal{T}_{v,yz}, \mathcal{T}_{w,yz}\}$, from which the eddy sizes in the crosswind plane can be estimated through the kite's crosswind speed. Such quantities are inaccessible to conventional fixed-point measurement techniques and difficult to obtain from single remote-sensing devices (due to their spatial averaging, which increases with height), reinforcing the potential of AWES as turbulence sensor. Moreover, the helical path allows estimation of the streamwise integral time scale $\mathcal{T}_{u,x}$ by using the nearly-periodic autocorrelation peaks for each looping period, as the kite sweeps approximately the same area in the y-z plane after completing a loop. The resultant $\mathcal{T}_{u,x}$ has been shown to be consistent with that obtained by sampling over return-phase trajectory. An additional time scale has been derived from the decay of the ACF peak-valley difference across successive loops, $\mathcal{T}_{u,T/2}$, which captures decorrelation between opposite sides of the production loop. This parameter captures the averaging effect of the turbulence across AWES loops, i.e., in aggregate from one side of a loop to the other, relevant for real-time adaptive control of AWES in turbulence; it is also theoretically relatable to the spatial cross-covariance (relegated to future work). Lastly, the spectra obtained in the production phase shows a clear peak at the looping frequency, demonstrating the effect of the trajectory on the sensed spectra. This also shows that another processing step is needed in order to use AWES for measuring turbulence spectra on a helical path. Note that for a horizontally-oriented helix, this is equivalent to sampling the flow that a conventional turbine blade encounters, involving ongoing and future work.

Overall, the results from both the return and production phases demonstrate that an AWES can provide meaningful turbulence measurements throughout the pumping cycle. As the two phases sample the flow differently, they provide complementary turbulence characteristics, illustrating the potential of AWES as atmospheric turbulence sensing platforms operating above the reach of conventional in-situ measurement systems. Moreover, a significant advantage over lidar is that AWES allows smaller spatial and temporal averaging scales, which can also be modified through the flight trajectory. Furthermore, lidar's sampling volume inherently increases at high altitudes, degrading its ability to measure turbulence at scales smaller than its averaging volumes.

A recommendation for future work is to validate the methodology through real AWES operational data. This would allow inference of the effect of sensor (e.g., pitot-tube) noise and uncertainty, and how to deal with such; it would use measurements instead of simulated turbulence through the Mann model. Multi-lidar measurements sampling the same path as an operational

https://doi.org/10.5194/wes-2026-150
Preprint. Discussion started: 18 September 2026

AWES would be ideal for this purpose (following, e.g., Berg et al., 2015; Wildmann et al., 2018). Moreover, the mean wind speed subtraction will be extended to account for wind shear in real operation, which was excluded from the present study.

Appendix A: Spectra of the turbulence signal in the return phase

Figure A1 shows the smoothed power spectral density for the three turbulence components sampled during the return phase. The smoothing via logarithmic bin-averaging is illustrated, along with the characteristic energy decay at high frequencies ($f > 0.3\,\mathrm{Hz}$). A reference line with slope $-5/3$ on the log-log axes, i.e. $S_{\beta\beta} \propto f^{-5/3}$, confirms that the spectra follow Kolmogorov's $-5/3$ law.

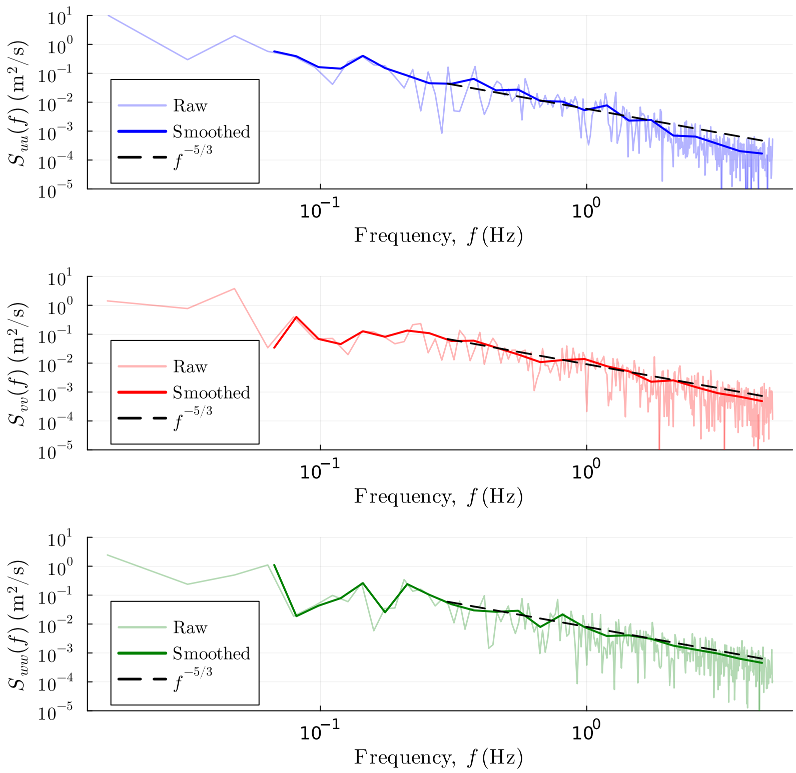

Figure A1. One-sided frequency-domain PSD $S_{uu}(f)$, $S_{vv}(f)$, and $S_{ww}(f)$ of turbulence fluctuations during the return phase, smoothed by logarithmic binning.

Appendix B: Taylor's hypothesis validation with a spiral flight

To further assess the role of the sampling strategy on the applicability of Taylor's hypothesis, a spiralling non-tethered flight trajectory is considered here. This flight path is not particular to AWES operation but it used as it combines streamwise and

https://doi.org/10.5194/wes-2026-150
Preprint. Discussion started: 18 September 2026

crosswind flight, and it would be applicable to real operations with Kitemill's system. The same procedure followed for the return phase in Section 4.1 is employed here. The spiralling trajectory consists of the untethered kite gliding down in spiral manoeuvres with the wind, i.e. the spiral follows the streamwise wind speed, as shown in Figure B1. Both the turbulence signal in time series and x series are required to validate the Taylor's hypothesis. However, for this sampling strategy, the x-component of the kite relative to the wind field is not monotonically increasing/decreasing, requiring sorting the x series prior to the interpolation to a uniform Δx. The sorting, however, eliminates the similarity between the spatial signal and the time signal on which the Taylor's hypothesis is based. To exemplify the sorting issue: a turbulence signal very close in x could be very distant in time, since the same x relative to the wind field is swept multiple times. This has been addressed by splitting the spiral trajectory in three segments, where the x component increases monotonically in each segment, as shown in the 3D trajectory, in Figure B1. This fragmentation makes the sorting not necessary. The kite position and velocity in NED over time for the three segments are shown in Figures B2 and B3 respectively.

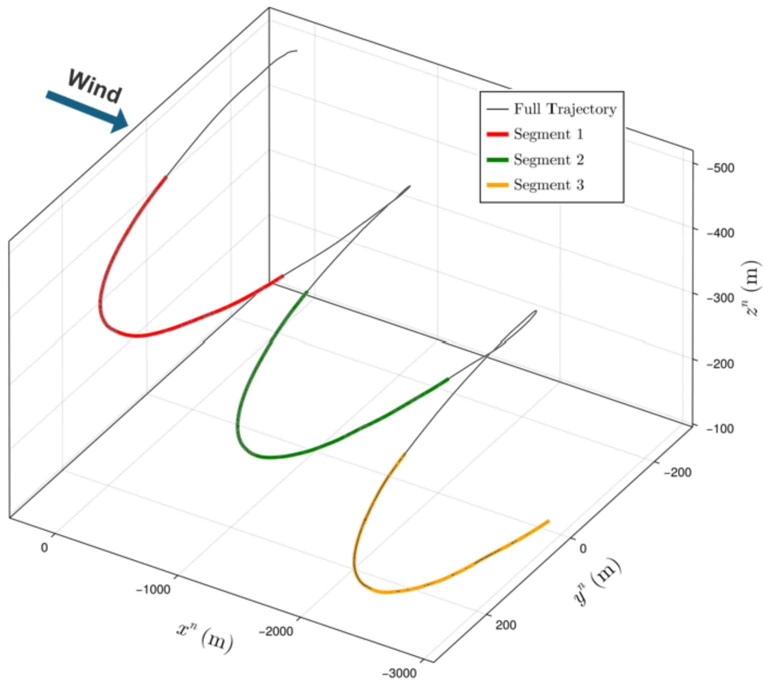

Figure B1. 3D plot of the kite trajectory during the spiral flight, split into three segments.

https://doi.org/10.5194/wes-2026-150
Preprint. Discussion started: 18 September 2026

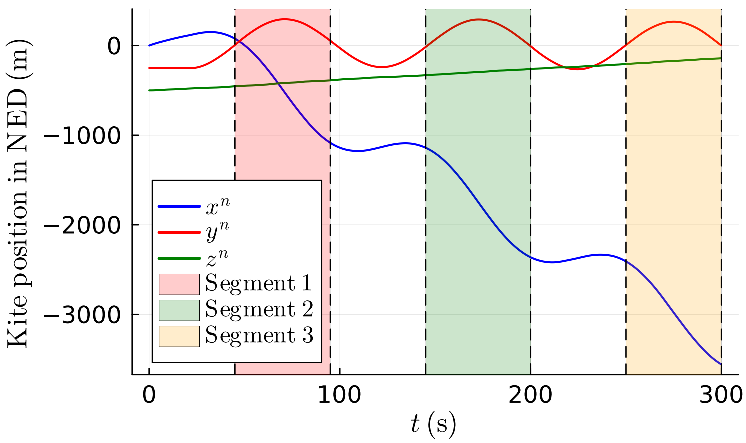

Figure B2. Kite position components in the NED frame during the spiral flight, with the three segments indicated.

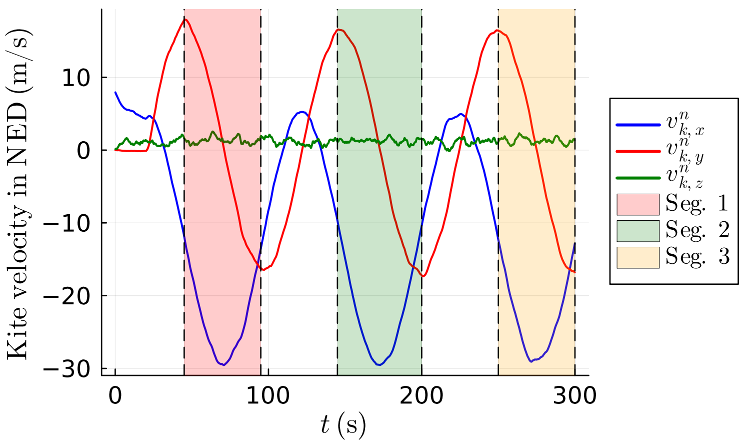

Figure B3. Kite velocity components in the NED frame during the spiral flight, with the three segments indicated.

The ACF is computed individually for each segment, for both time series and x-series, from which the integral length and time scales are obtained. Such values are provided in Table B1 for the three segments separately. The obtained integral length scale to time scale ratios would give the streamwise relative kite speed if Taylor's hypothesis was applicable, however a significant discrepancy is present. From such discrepancy it is inferred that the Taylor's hypothesis cannot be employed to compute the length scales from time scales for such sampling strategy. The discrepancy arises because Taylor's hypothesis assumes the sampling is aligned with the streamwise direction, so that a temporal lag τ maps to a streamwise spatial lag. In the spiral trajectory, however, the kite has a significant crosswind velocity component $v_{k,yz}$, thus, consecutive samples are separated in both the streamwise and crosswind directions. The measured autocorrelation then mixes both directions,

https://doi.org/10.5194/wes-2026-150
Preprint. Discussion started: 18 September 2026

eawe european academy of wind energy
Open Access WIND ENERGY SCIENCE DISCUSSIONS

which have different characteristic scales, and the ratio $\mathcal{L}/\mathcal{T}$ no longer recovers the streamwise relative kite speed. Table B1 provides the results for the streamwise component although the same conclusion would be inferred from the lateral and vertical components.

Table B1. Integral length and time scales for the streamwise component per spiral segment, and their ratio compared to the mean streamwise relative kite speed, $\bar{v}_{r,x}$.

Segment	$\mathcal{L}_u$ (m)	$\mathcal{T}_u$ (s)	$\mathcal{L}_u/\mathcal{T}_u$ (m/s)	$\bar{v}_{r,x}$ (m/s)	Relative deviation (%)
1	38.24	3.09	12.38	10.82	14.42
2	42.43	3.76	11.28	9.68	16.53
3	32.44	2.34	13.86	10.78	28.57

The Taylor's hypothesis non-validity for this sampling strategy can be also assessed by computing the ratio of wavenumber-domain PSD to frequency-domain PSD, as was done in Section 4.1. Figure B4 shows the ratio for the three components for the three different segments compared to the value that Taylor's hypothesis would dictate.

https://doi.org/10.5194/wes-2026-150
Preprint. Discussion started: 18 September 2026

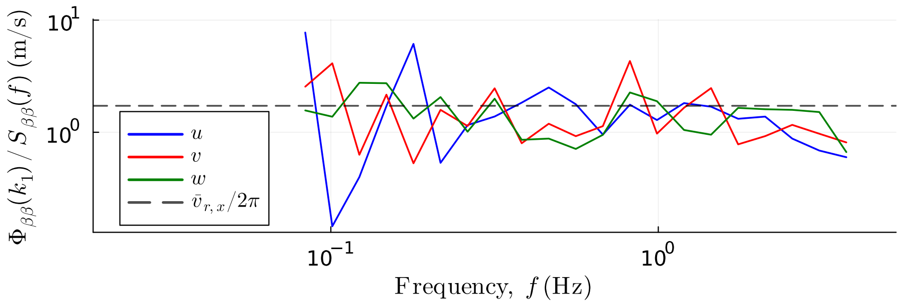

(a) Segment 1

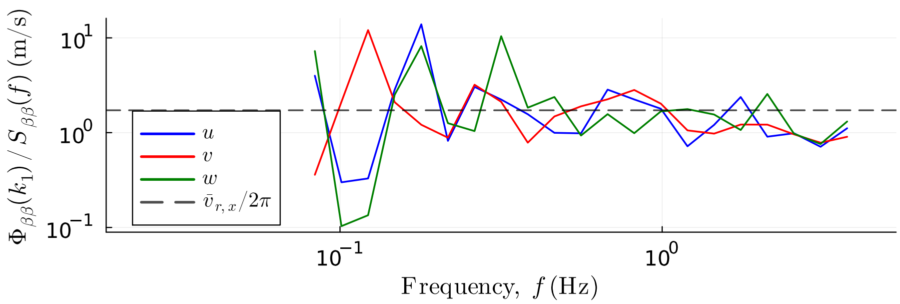

(b) Segment 2

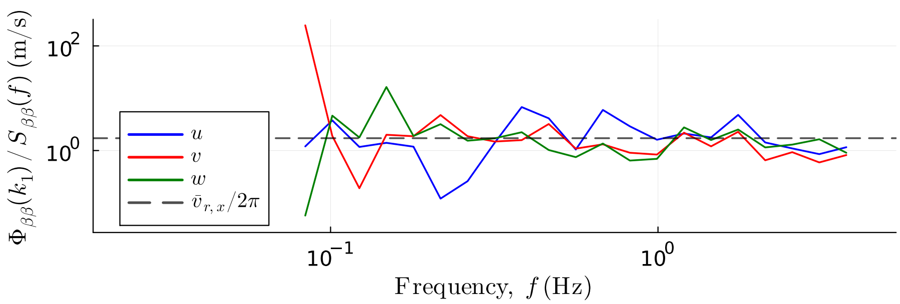

(c) Segment 3

Figure B4. Ratio $\Phi_{\beta\beta}(k_1)/S_{\beta\beta}(f)$ for the three turbulence components during the spiral flight for segments 1, 2, and 3, compared to the expected value $\bar{v}_{r,x}/(2\pi)$ (dashed line) according to Taylor's hypothesis.

Figure B4 confirms through the spectral approach that the Taylor's hypothesis does not hold for the spiral sampling strategy. The ratio $\Phi(k_1)/S(f)$ deviates substantially from the expected value $\bar{v}_{r,x}/(2\pi)$ for all three segments and the three turbulence components (note the logarithmic y axis), in contrast to the return-phase results in Figure 14. This is consistent with the table results above, as argued, the dominant crosswind velocity component in the spiral trajectory causes the temporal and spatial series to sample different characteristic scales, so the ratio $\Phi(k_1)/S(f)$ no longer recovers the streamwise relative kite speed as Taylor's hypothesis would predict. It is inferred that trajectory geometry, i.e. sampling strategy, must be considered before

https://doi.org/10.5194/wes-2026-150
Preprint. Discussion started: 18 September 2026

applying the Taylor's hypothesis. This also confirms that the crosswind-dominated sampling strategy of the production phase is likewise incompatible with Taylor's hypothesis, as argued in Section 4.2.

Appendix: Nomenclature

Velocity vectors and components

$\boldsymbol{v_w} = [u, v, w]^\top$	Wind velocity vector and its streamwise, lateral, vertical components ($\mathrm{m\,s^{-1}}$)
$\boldsymbol{v_r} = [v_{r,x}, v_{r,y}, v_{r,z}]^\top$	Relative kite velocity vector and its streamwise, lateral, vertical components ($\mathrm{m\,s^{-1}}$)
$\boldsymbol{v_k} = [v_{k,x}, v_{k,y}, v_{k,z}]^\top$	Kite velocity vector and its streamwise, lateral, vertical components ($\mathrm{m\,s^{-1}}$)
$\boldsymbol{v_a} = [v_{a,x}, v_{a,y}, v_{a,z}]^\top$	Apparent wind velocity vector and its streamwise, lateral, vertical components ($\mathrm{m\,s^{-1}}$)
$\boldsymbol{\omega}_b = [p, q, r]^\top$	Body angular velocity vector and its roll, pitch, yaw rate components ($\mathrm{deg\,s^{-1}}$)
V_a	Airspeed, magnitude of $\boldsymbol{v_a}$ and $\boldsymbol{v_r}$ ($\mathrm{m\,s^{-1}}$)
U	Mean streamwise wind speed ($\mathrm{m\,s^{-1}}$)
$v_{k,yz}$	Kite crosswind speed magnitude ($\mathrm{m\,s^{-1}}$)

Turbulence fluctuations and intensity

u', v', w'	Turbulence velocity fluctuations, streamwise, lateral, vertical ($\mathrm{m\,s^{-1}}$)
σ_u	Standard deviation of streamwise turbulence fluctuation ($\mathrm{m\,s^{-1}}$)
I_u, I_v, I_w	Turbulence intensity, streamwise, lateral, vertical (-)
σ^2	Variance of turbulence signal ($\mathrm{m^2\,s^{-2}}$)

Autocorrelation and integral scales

ρ	Autocorrelation function (ACF) (-)
τ	Time lag (s)
$\mathcal{T}_u$, $\mathcal{T}_v$, $\mathcal{T}_w$	Integral time scales, streamwise, lateral, vertical (s)
$\mathcal{T}_{u,yz}$, $\mathcal{T}_{v,yz}$, $\mathcal{T}_{w,yz}$	Crosswind integral time scales (s)
$\mathcal{T}_{u,x}$	Streamwise integral time scale (s)
$\mathcal{T}_{u,T/2}$	Half-period integral time scale (s)
$\mathcal{L}_u$, $\mathcal{L}_v$, $\mathcal{L}_w$	Integral length scales, streamwise, lateral, vertical (m)
$\mathcal{L}_{u,yz}$, $\mathcal{L}_{v,yz}$, $\mathcal{L}_{w,yz}$	Crosswind integral length scales (m)

https://doi.org/10.5194/wes-2026-150
Preprint. Discussion started: 18 September 2026

Spectral quantities

$S_{uu}(f)$, $S_{vv}(f)$, $S_{ww}(f)$	One-sided frequency-domain power spectral density ($\mathrm{m^2\,s^{-1}}$)
$\Phi_{uu}(k_1)$, $\Phi_{vv}(k_1)$, $\Phi_{ww}(k_1)$	One-sided wavenumber-domain power spectral density ($\mathrm{m^3\,s^{-2}}$)
$\hat{u}(f)$	Discrete Fourier transform of u'
f	Frequency (Hz)
f_s	Sampling frequency (Hz)
k_1	Streamwise radial wavenumber ($\mathrm{rad\,m^{-1}}$)
κ	Streamwise cyclic wavenumber ($\mathrm{cycles\,m^{-1}}$)
N	Number of samples (-)
Δt	Temporal sampling interval (s)
Δx	Spatial sampling interval (m)

Mann model parameters

L_{MM}	Length scale, size of energy-containing eddies (m)
$\alpha_{\mathrm{MM}}\varepsilon^{2/3}$	Energy dissipation rate parameter ($\mathrm{m^{4/3}\,s^{-2}}$)
ε	Viscous dissipation rate of turbulent kinetic energy ($\mathrm{m^2\,s^{-3}}$)
α_{MM}	Kolmogorov spectral constant (-)
Γ	Anisotropy parameter (-)
Δx_{MM}, Δy_{MM}, Δz_{MM}	Turbulence box cell dimensions (m)

Aerodynamic coefficients and angles

C_D, C_Y, C_L	Drag, side force, lift coefficients (-)
C_l, C_m, C_n	Roll, pitch, yaw moment coefficients (-)
α	Angle of attack (deg)
β	Sideslip angle (deg)

Reference frames and coordinates

NED	North-East-Down reference frame
x, y, z	Streamwise, lateral, vertical coordinates (m)
R_b^n	Rotation matrix from body frame to NED frame (-)
R_w^b	Rotation matrix from wind frame to body frame (-)

Code and data availability. The simulation model and data is proprietary and is therefore not available for the public.

https://doi.org/10.5194/wes-2026-150
Preprint. Discussion started: 18 September 2026

Author contributions. Conceptualization: AP and MK; methodology: AP and MK; software: AP, EO, and DN; writing – original draft preparation: AP and MK; writing – review and editing: AP, MK, DN, and EO; supervision: MK and EO; funding acquisition: MK and EO. All authors have read and agreed to the published version of the manuscript.

Competing interests. The authors declare that they have no conflict of interest.

Acknowledgements. The authors gratefully acknowledge Kitemill AS for providing access to their in-house simulator environment, Universal Simulator for Airborne Wind Energy (UniSimAWE) and to their test site Lidar data. We acknowledge the use of OpenAI's ChatGPT for assistance in refining the writing style of this paper.

Financial support. This work has been supported by the AWETRAIN project, which receives funding from the European Union's Horizon Europe research and innovation programme under the Marie Skłodowska-Curie grant agreement No 101168734. Duc H. Nguyen is supported by the UK Engineering and Physical Sciences Research Council (EPSRC), grant number EP/Y014545/1.

https://doi.org/10.5194/wes-2026-150
Preprint. Discussion started: 18 September 2026

References

Berg, J., Vasiljevic, N., Kelly, M., Lea, G., and Courtney, M.: Addressing Spatial Variability of Surface-Layer Wind with Long-Range WindScanners, Journal of Atmospheric and Oceanic Technology, 32, 518–527, https://doi.org/10.1175/JTECH-D-14-00123.1, 2015.

Cayon, O., Watson, S., and Schmehl, R.: Kite as a sensor: wind and state estimation in tethered flying systems, Wind Energy Science, 10, 2161–2188, https://doi.org/10.5194/wes-10-2161-2025, 2025.

Cherubini, A., Papini, A., Vertechy, R., and Fontana, M.: Airborne Wind Energy Systems: A review of the technologies, Renewable and Sustainable Energy Reviews, 51, 1461–1476, https://doi.org/10.1016/j.rser.2015.07.053, 2015.

de Mare, M. and Mann, J.: On the Space-Time Structure of Sheared Turbulence, Boundary-Layer Meteorology, 160, 453–474, https://doi.org/10.1007/s10546-016-0143-z, 2016.

Dimitrov, N., Pedersen, M., and Hannesdóttir, : An open-source Python-based tool for Mann turbulence generation with constraints and non-Gaussian capabilities, in: Journal of Physics: Conference Series, vol. 2767, p. 052058, IOP Publishing, https://doi.org/10.1088/1742-6596/2767/5/052058, 2024.

Eberhard, W. L., Cupp, R. E., and Healy, K. R.: Doppler Lidar Measurement of Profiles of Turbulence and Momentum Flux, Journal of Atmospheric and Oceanic Technology, 6, 809–819, https://doi.org/10.1175/1520-0426(1989)006<0809:dlmopo>2.0.co;2, 1989.

Eijkelhof, D., Rossi, N., and Schmehl, R.: Optimal flight pattern debate for airborne wind energy systems: circular or figure of eight?, Wind Energy Science, 11, 1287–1304, https://doi.org/10.5194/wes-11-1287-2026, 2026.

Fagiano, L., Quack, M., Bauer, F., Carnel, L., and Oland, E.: Autonomous airborne wind energy systems: accomplishments and challenges, Annual Review of Control, Robotics, and Autonomous Systems, 5, 603–631, https://doi.org/10.1146/annurev-control-042820-124658, 2022.

International Electrotechnical Commission: IEC Standard 61400–1, Edition 4. Wind turbine generator systems — Part 1: Design requirements, Tech. rep., IEC, 2020.

Kelly, M.: From standard wind measurements to spectral characterization: turbulence length scale and distribution, Wind Energy Science, 3, 533–543, https://doi.org/10.5194/wes-3-533-2018, 2018.

Kelly, M.: Flow acceleration statistics: a new paradigm for wind-driven loads, towards probabilistic turbine design, Wind Energy Science, 10, 535–558, https://doi.org/10.5194/wes-10-535-2025, 2025.

Lumley, J.: Interpretation of time spectra measured in high-intensity shear flows, The physics of fluids, 8, 1056–1062, https://doi.org/10.1063/1.1761355, 1965.

Mann, J.: The spatial structure of neutral atmospheric surface-layer turbulence, Journal of Fluid Mechanics, 273, 141–168, https://doi.org/10.1017/S0022112094001886, 1994.

Mann, J.: Wind Field Simulation, Probabilistic Engineering Mechanics, 13, 269–282, https://doi.org/10.1016/s0266-8920(97)00036-2, 1998.

Nguyen, D. H., Porta Ko, A., Tveide, T., Lowenberg, M. H., and Oland, E.: Controlling rigid-wing airborne wind energy systems during circular flight without exact path following, Wind Energy Science, 11, 2987–3013, https://doi.org/10.5194/wes-11-2987-2026, 2026.

Petersen, J. T., Kretz, A., and Mann, J.: Influence of transversal turbulence on lifetime predictions for a HAWT, Contributions from the Department of Meteorology and Wind Energy to the EWEC, 94, 72, 1995.

Peña, A., Yankova, G. G., and Mallini, V.: On the lidar-turbulence paradox and possible countermeasures, Wind Energy Science, 10, 83–102, https://doi.org/10.5194/wes-10-83-2025, 2025.

https://doi.org/10.5194/wes-2026-150
Preprint. Discussion started: 18 September 2026

Rackauckas, C. and Nie, Q.: Differentialequations. jl–a performant and feature-rich ecosystem for solving differential equations in julia, Journal of open research software, 5, 15–15, https://doi.org/10.5334/jors.151, 2017.

Ranneberg, M.: Sensor Setups for State and Wind Estimation for Airborne Wind Energy Converters, https://doi.org/10.48550/arXiv.1309.1029, 2013.

Schmidt, E., De Lellis, M., Saraiva, R., and Trofino, A.: State Estimation of a Tethered Airfoil for Monitoring, Control and Optimization., IFAC-PapersOnLine, 50, 13 246–13 251, https://doi.org/10.1016/j.ifacol.2017.08.1960, 20th IFAC World Congress, 2017.

Schmidt, E., De Lellis Costa de Oliveira, M., Saraiva da Silva, R., Fagiano, L., and Trofino Neto, A.: In-Flight Estimation of the Aerodynamics of Tethered Wings for Airborne Wind Energy, IEEE Transactions on Control Systems Technology, 28, 1309–1322, https://doi.org/10.1109/TCST.2019.2907663, 2020.

Smalikho, I. N. and Banakh, V. A.: Measurements of wind turbulence parameters by a conically scanning coherent Doppler lidar in the atmospheric boundary layer, Atmospheric Measurement Techniques, 10, 4191–4208, https://doi.org/10.5194/amt-10-4191-2017, 2017.

Stengel, R. F.: Flight dynamics, Princeton university press, 2022.

Taylor, G. I.: The statistical theory of isotropic turbulence, Journal of the Aeronautical Sciences, 4, 311–315, https://doi.org/10.2514/8.419, 1937.

Taylor, G. I.: The Spectrum of Turbulence, Proceedings of the Royal Society of London. Series A, 164, 476–490, https://doi.org/10.1098/rspa.1938.0032, 1938.

Tong, C. and Wyngaard, J.: Two-point coherence in the atmospheric surface layer, Boundary-layer meteorology, 81, 105–121, https://doi.org/10.1007/BF00119061, 1996.

Van Der Vlugt, R., Peschel, J., and Schmehl, R.: Design and experimental characterization of a pumping kite power system, in: Airborne Wind Energy, pp. 403–425, Springer, Berlin, Heidelberg, https://doi.org/10.1007/978-3-642-39965-7_23, 2013.

Wildmann, N., Vasiljevic, N., and Gerz, T.: Wind turbine wake measurements with automatically adjusting scanning trajectories in a multi-Doppler lidar setup, Atmospheric Measurment Techniques, 11, 3801–3814, https://doi.org/10.5194/amt-2018-55, 2018.

Wyngaard, J. and Clifford, S.: Taylor's hypothesis and high–frequency turbulence spectra, Journal of Atmospheric Sciences, 34, 922–929, https://doi.org/10.1175/1520-0469(1977)034<0922:THAHTS>2.0.CO;2, 1977.